Probing an ultralight QCD axion with electromagnetic quadratic interaction

Hyungjin Kim and Alessandro Lenoci⬤

Deutsches Elektronen-Synchrotron DESY, Notkestrasse 85, 22607 Hamburg, Germany

Gilad Perez and Wolfram Ratzinger⬤

Department of Particle Physics and Astrophysics, Weizmann Institute of Science, Rehovot 7610001, Israel

The axion-gluon coupling is the defining feature of the QCD axion. This feature induces additional and qualitatively different interactions of the axion with standard model particles—quadratic couplings. Previously, hadronic quadratic couplings have been studied and experimental implications have been explored especially in the context of atomic spectroscopy and interferometry. We investigate additional quadratic couplings to the electromagnetic field and electron mass. These electromagnetic quadratic couplings are generated at the loop level from threshold corrections and are expected to be present in the absence of fine-tuning. While they are generally loop-suppressed compared to the hadronic ones, they open up new ways to search for the QCD axion, for instance via optical atomic clocks. Moreover, due to the velocity spread of the dark matter field, the quadratic nature of the coupling leads to low-frequency stochastic fluctuations. These distinctive low-frequency fluctuations offer a new way to search for heavier axions. We provide an analytic expression for the power spectral density of this low-frequency background and briefly discuss experimental strategies for a low-frequency stochastic background search.

I. INTRODUCTION

The axion ssolution of the strong *CP* problem requires the axion field to couple to the strong sector [1–8]. Couplings between ultralight spin-0 fields and the strong sector occur also in models addressing other theoretical questions, such as the quark-flavor puzzle and electroweak hierarchy problem, or in phenomenological models like the Higgs-portal [9–18]. If the spin-0 field is a scalar, these couplings are severely constrained by equivalence-principle and fifth-force bounds [19,20]. Conversely, if the spin-0 field is a pseudoscalar field, long-range forces do not appear at the leading order, and therefore, the corresponding bounds are dramatically weaker.

[These ultralight states could account for the dark matter in the present universe. The canonical example is the QCD axion dark matter [21–23], where the coherent oscillation of the axion plays a role of cold dark matter. On the more phenomenological side, fuzzy dark matter of mass $m \simeq 10^{-22}$ eV was proposed to resolve problems of cold dark matter at small scales [24]. Currently, no positive signals of ultralight dark matter (ULDM) candidates exist,

resulting in bounds on its mass and on possible interactions between ULDM and the standard model (SM) particles. For instance, astrophysical and cosmological investigations have placed a lower bound on the ULDM mass as $m \gtrsim 10^{-19} - 10^{-20}$ eV (see Ref. [25] for a recent review).]

Current terrestrial axion dark matter searches mostly rely on its anomalous coupling to the photon or axial-vector couplings to standard model particles. However, below the confinement scale, strong confining dynamics generate sizable quadratic couplings of the QCD axion to SM scalar operators in the strong sector,[1] offering new directions for axion searches. For instance, the quadratic couplings can change the potential structure of the axion in a finite density environment, which can be examined in extreme stellar environments such as white dwarfs and neutron stars [27–30].

Moreover, these hadronic quadratic couplings induce small time-oscillations of nuclear parameters, if the axion constitutes the observed dark matter. Such small oscillations of nuclear parameters can be probed by atomic spectroscopy and/or interferometry, for instance by atomic clocks [31]. While atomic spectroscopy provides an interesting way to probe axion dark matter, it is still challenging to probe the axion via hadronic quadratic couplings since

---

[1]In generic axion models these are suppressed by the axion mass [26].
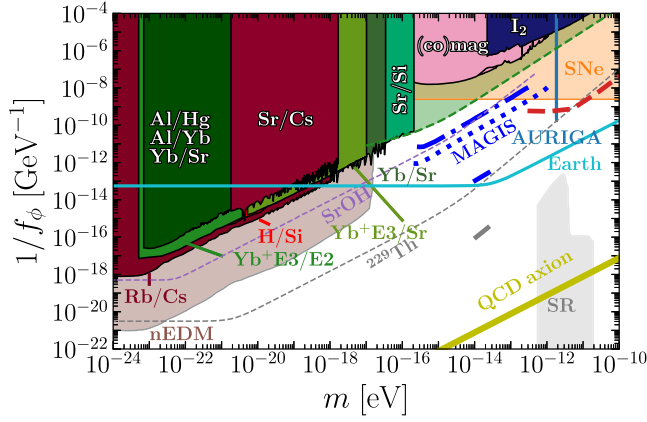
FIG. 1. Summary of constraints. Constraints with microwave clocks are shown in a red color scheme: Rb/Cs fountain clocks (Rb/Cs) [32], a H-maser with a Si cavity (H/Si) [33], and strontium and cesium clocks (Sr/Cs) [34]. They receive the dominant contribution from the variation of nuclear parameters [31]. Constraints based on optical transitions are shown with a green color scheme: Yb$^+$ and Sr (Yb/Sr) [34], Sr with a Si cavity (Sr/Si) [33], Al$^+$, Hg$^+$, Yb, and Sr (Al/Hg, Al/Yb, Yb/Sr) [35], and the electric-octupole (E3) and the electric-quadrupole (E2) transitions of Yb$^+$ ion (Yb$^+$E3/E2), and Yb$^+$ (E3) and Sr (Yb$^+$E3/Sr) [36]. The region bounded by the green dashed line is excluded by comparing measured frequency uncertainties in Yb$^+$E3/E2 with the low-frequency fluctuations of the axion DM (see Sec. IV for details). Other constraints and projections include: (co)magnetometers (pink) with a projection of NAS-DUCK (pink dashed) [37–40], molecular iodine I_2 spectroscopy (dark blue), MAGIS-100/MAGIS-km (dot-dashed/dotted blue), a projection of CASPEr-electric (red dashed) [41], the AURIGA resonant bar gravitational wave experiment (emerald) [42], oscillating neutron EDM (brown) [43], supernova 1987A (orange) [44], axion superradiance constraints (gray) [45], ^{229}Th nuclear isomer transition (gray dashed) [14,46], and strontium monohydroxide SrOH (violet dashed) [47]. We also show a minimal QCD axion line (olive), corresponding to $m^2 f_\phi^2 \simeq m_\pi^2 f_\pi^2$. Spectroscopy bounds above the cyan solid line must be taken carefully as the axion could develop a static profile around the Earth (cyan) [27]. In addition, we show the reaches of MAGIS-km and ^{229}Th nuclear clock as a thick blue and gray line in scenarios where the DM density in the solar system is enhanced via capture processes [48]. Constraints from magnetometers and supernova are obtained by assuming axion-nucleon couplings from KSVZ-like QCD axion models [49].

atomic clocks are in general less sensitive to the variation of nuclear parameters.

In this work, we explore another kind of quadratic interaction of the QCD axion—the quadratic interactions with the electromagnetic field and the electron. The former arises from one-loop corrections, while the latter is induced by two-loop corrections. Although such couplings are generally smaller than their hadronic counterpart, they allow us to probe the QCD axion with a wider range of experimental setups, some of which are more sensitive.

These couplings are induced and dominated by loops involving IR states and therefore are expected to be naturally present in the theory regardless of the details of the microscopic theory. The main objective of this work is to study the interplay between current and near-future experimental sensitivity of the quadratic axion couplings to the strong and electromagnetic sectors. Our main result, which will be detailed below, is summarized in Fig. 1.

This work is organized as follows. In Sec. II, we briefly discuss hadronic quadratic couplings from the axion-gluon interaction. We then show that the hadronic quadratic couplings generate quadratic interactions with the photon and the electron at one and two-loop levels, respectively. In Sec. III, we discuss the implications of electromagnetic quadratic interactions in axion searches with atomic spectroscopy and gravitational wave detectors. In Sec. IV, we discuss in more detail the signal spectrum of axion dark matter generated by quadratic interactions. We show that the quadratic nature of the coupling leads to low-frequency stochastic fluctuations of observables besides the coherent harmonic signals at frequencies corresponding to two times the axion mass. We further discuss possibilities to constrain and probe such stochastic signals in an experimental setup with a single detector and multiple detectors. We conclude in Sec. V. We use natural units $c = \hbar = 1$ throughout this work.

II. QUADRATIC COUPLINGS

We start from the axion coupling to the standard model gluon field,

$$\mathcal{L} = \frac{g_s^2}{32\pi^2} \frac{\phi}{f_\phi} G_{\mu\nu}^a \tilde{G}^{a\mu\nu}, \tag{1}$$

where f_ϕ is the axion decay constant, g_s is the strong coupling, $G_{\mu\nu}^a$ and $\tilde{G}_{\mu\nu}^a$ are the gluon field strength and its dual. We do not take into account any other couplings in this work; i.e. we consider KSVZ-like models where axion couplings to the axial vector currents of SM fields are absent at UV scales. Model-dependent couplings will not change our analysis, but they may lead to additional bounds on the axion parameter space.

The axion-gluon coupling (1) naturally leads to hadronic quadratic couplings below the QCD scale. For instance, the pion mass can be found from the chiral Lagrangian as $m_\pi^2(\theta) = B(m_u^2 + m_d^2 + 2m_u m_d \cos\theta)^{1/2}$ with $B = -\langle \bar{q}q \rangle_0 / f_\pi^2$ and $\theta = \phi/f_\phi$ [50,51]. Expanding the pion mass around $\theta = 0$, we find a quadratic coupling to pions, $\mathcal{L} \supset \theta^2 \pi^2$. Furthermore, the nucleon mass depends on the pion mass through $\mathcal{L} \supset 4c_1 m_\pi^2(\theta)\bar{N}N$ with $c_1 = -1.1$ GeV^{-1} [52], which leads to a quadratic interaction between the axion and nucleons as well.

The hadronic quadratic interactions introduce time oscillations of the nuclear parameters if the axion is the
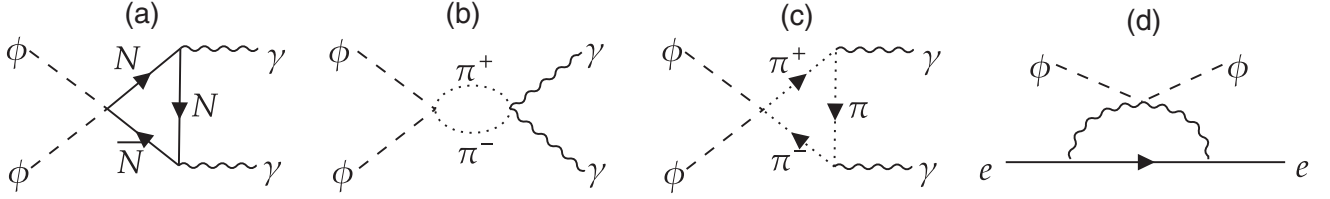
FIG. 2.   The Feynman diagrams that are responsible for the quadratic operators of the axion to the electromagnetic field Eq. (3) [diagrams (a), (b), and (c)] and to electrons Eq. (8) [diagram (d)]. In the diagram (d), the vertex between axions and photons is obtained from the other three diagrams.

dark matter in the present universe. As it is clear from the chiral Lagrangian, the pion and nucleon mass will receive a small oscillating component, e.g.

$$\frac{\delta m_\pi^2}{m_\pi^2} = -\frac{z}{2(1+z)^2}\theta^2(t) \qquad (2)$$

with $z = m_u/m_d$. The amplitude of the oscillating $\theta^2(t)$ is proportional to the dark matter density $\rho \approx \theta^2(t)m^2 f_\phi^2$, where m denotes the axion mass. Other nuclear parameters that depend on the pion mass, such as the nuclear g-factor will also receive such a time-oscillating component. As a consequence, atomic energy levels oscillate and, in addition, any object whose mass receives QCD contributions experiences an acceleration due to the axion dark matter background.

Based on this observation, it was shown in Ref. [31] that spectroscopic and interferometric measurements, such as atomic clocks and gravitational wave interferometers, can be used to search the axion at the low mass range. In particular, clock comparison tests using hyperfine transitions are considered since hyperfine transitions are directly affected by the variation of nuclear parameters. In addition, gravitational wave interferometers are considered as most mass of the test bodies comes from QCD, and therefore, they fluctuate inevitably in the axion dark matter background.

[Furthermore, as we will show shortly, the hadronic interactions also lead to EM quadratic couplings at low energy scales through loop corrections. A small change in the charged pion mass due to the background axion dark matter inevitably introduces a fluctuation of the quantum corrections to the fine structure constant and the electron mass. These effects can be described as electromagnetic quadratic operators of axions, and will allow us to utilize a broader range of spectroscopic measurements for the axion search. Below, we detail how these EM couplings are induced and show that all of these effects are due to the variation of the pion mass.]

A. Quadratic interaction with the electromagnetic field

We first consider the quadratic coupling to the electromagnetic field,

$$\mathcal{L} = -\frac{1}{4}F_{\mu\nu}F^{\mu\nu} + \frac{C_\gamma}{4}\frac{\phi^2}{f_\phi^2}F_{\mu\nu}F^{\mu\nu} \qquad (3)$$

at energy scales below the pion mass. The coefficient C_γ is given as

$$C_\gamma = -\frac{z}{24(1+z)^2}\frac{\alpha}{\pi}\left(1 + 8\frac{\sigma_{\pi N}}{m_N}\right) \simeq -3 \times 10^{-5}. \qquad (4)$$

Here $z = m_u/m_d \simeq 0.46$ and $\sigma_{\pi N} = \partial m_N/\partial \ln m_\pi^2 \sim \mathcal{O}(50)$ MeV. The coefficient C_γ can be directly obtained from the one-loop computation of $\phi\phi \to \gamma\gamma$ via a pion loop or a nucleon loop as shown in diagrams (a), (b) and (c) in Fig. 2. Alternatively, it can be read off from the threshold correction to the running of the fine structure constant with respect to the variation of the pion and the nucleon masses.

Consider the running of the electromagnetic coupling $1/e^2$ from $\Lambda_{\rm UV}$ to $\Lambda_{\rm IR}$. Let us assume a single charged particle whose mass m_π is in between these scales. The gauge coupling runs as $1/e^2(\Lambda_{\rm IR}) - 1/e^2(\Lambda_{\rm UV}) = \int_{\Lambda_{\rm IR}}^{\Lambda_{\rm UV}} d\ln\mu[2\beta_e(\mu)/e^3]$ where $\beta_e(\mu) = (be^3/8\pi^2)$, $b = \frac{2}{3}\sum_f Q_f^2 + \frac{1}{6}\sum_s Q_s^2$, and the sums over f and s account for Dirac fermions and complex scalars, respectively. For a fixed UV value of the gauge coupling, one finds that the gauge coupling at low energy depends on the mass of the charged particle,

$$\delta\left(\frac{1}{e_{\rm IR}^2}\right) = -\frac{\Delta b}{4\pi^2}\frac{\delta m_\pi}{m_\pi}. \qquad (5)$$

Here Δb is the change of the beta function coefficient at the threshold; $\Delta b = 2Q^2/3, Q^2/6$ for a Dirac fermion and a complex scalar field of charge Q, respectively. In the effective Lagrangian, this dependence is incorporated by

$$\mathcal{L} = \frac{\Delta b e^2}{(4\pi)^2}\frac{\delta m_\pi}{m_\pi}F_{\mu\nu}F^{\mu\nu}.$$

From this, we obtain

$$\frac{\delta\alpha}{\alpha} = C_\gamma\theta^2 = \frac{\alpha}{\pi}\sum_i \Delta b_i \frac{\delta m_i}{m_i} = \frac{\alpha}{12\pi}\left[1 + \frac{8\sigma_{\pi N}}{m_N}\right]\frac{\delta m_\pi^2}{m_\pi^2}, \qquad (6)$$

where we include the variation of the nucleon mass; the fine structure constant fluctuates as the pion mass changes due to the background axion dark matter.

B. Quadratic interaction with electron mass

Furthermore, the hadronic quadratic couplings lead to a quadratic coupling to the electron mass,

$$\mathcal{L} = -C_e m_e \frac{\phi^2}{f_\phi^2} \bar{e}e, \tag{7}$$

where the coefficient C_e is

$$C_e \simeq \frac{3\alpha}{4\pi} C_\gamma \ln \frac{m_\pi^2}{m_e^2}. \tag{8}$$

This effect arises at two-loop order; it is suppressed by $(\alpha/\pi)^2$.

We estimate the coefficient C_e in the following way. Below the QCD scale, the dim-6 operator (3) contributes to the running of the electron mass. In QED, the correction to the electron mass due to running from the QCD scale to the electron mass is given by $(\delta m_e/m_e) = (3\alpha/4\pi) \ln m_\pi^2/m_e^2$. Since $\theta^2(t)$ oscillates at a frequency much smaller than the electron mass or the QCD scale, we can effectively take $C_\gamma\theta^2$ as a constant and absorb it by rescaling the gauge field $A_\mu \to (1 + C_\gamma\theta^2)^{1/2}A_\mu$. This is equivalent to taking $e^2 \to e^2(1 + C_\gamma\theta^2)$. Using the QED result, one finds that the dim-6 operator contributes to the running as

$$\frac{\delta m_e}{m_e} \simeq \frac{3\alpha}{4\pi} C_\gamma \theta^2 \ln(m_\pi^2/m_e^2) = C_e \theta^2$$

from which we estimate C_e as in (8). An explicit computation of the diagram (d) in Fig. 2 leads to the same estimation. However, we do not consider the variation of electron mass further as its effect on observables is usually much smaller than the variation of the fine structure constant and nuclear parameters.

III. IMPLICATIONS

The quadratic couplings to the electromagnetic field and the electron mass offer alternative ways to search for the QCD axion. Previously, Ref. [31] focused on the quadratic coupling to hadrons.[2] Assuming that the axion constitutes DM, it was pointed out that such hadronic quadratic couplings lead to time variations of the nuclear parameters, such as the nucleon mass and nuclear g-factor, and that atomic clocks based on hyperfine transitions could probe the axion DM-induced signals. With additional quadratic couplings to the electromagnetic field and the electron

---

[2]A generic ultralight dark matter model with ϕ^2 coupling was considered in [53,54].

mass, a wider range of experiments, e.g. atomic clocks based on electronic transitions, becomes sensitive to the QCD axion dark matter. Since such optical clocks usually have a shorter averaging time and better sensitivities, one can expect to probe a wider range of parameter space.

For clarification, let us briefly review how a clock comparison test probes couplings of ultralight dark matter with SM particles [46]. Consider two stable frequency standards f_A and f_B. Suppose that each frequency standard has a slightly different dependence on the fine structure constant, $f_A \propto \alpha^{\xi_A}$ and $f_B \propto \alpha^{\xi_B}$ with $\xi_A \neq \xi_B$. Due to the time-variation of the fine structure constant caused by the DM field, the ratio of these two frequencies fluctuates as

$$\frac{\delta(f_A/f_B)}{(f_A/f_B)} = (\xi_A - \xi_B)\frac{\delta\alpha}{\alpha} \propto \theta^2(t),$$

where $\theta^2(t) = (\rho_0/m^2 f_\phi^2)\cos(2mt)$ is related to $\delta\alpha/\alpha$ by (6). By monitoring the frequency ratio and investigating if the time series contains any harmonic signal at $\omega = 2m$, one can probe the QCD axion.

Generically the fractional frequency deviation arising from a quadratic coupling can be written as

$$\frac{\delta f_A}{f_A} = K_A \theta^2(t), \tag{9}$$

where K_A is the sensitivity coefficient that depends on the atomic species and transition. It takes all the effects (hadronic and electromagnetic) into account. A list of the coefficient K_A for different atom species is available in Appendix A.

Any stable frequency standard can be used to search for the QCD axion. Ref. [31] only used hyperfine transitions as only hadronic quadratic couplings were considered in that work and hadronic couplings do not affect the electronic transition to leading order. Possible variations of electronic transition caused by oscillations of the nuclear charge radius were investigated in Ref. [55]. Due to the electromagnetic quadratic couplings described above, electronic transition levels now change directly as the background DM oscillates. Although these new quadratic couplings are at least one-loop suppressed, they still lead to competitive bounds compared to microwave clocks as optical clocks have orders of magnitude smaller frequency uncertainties.

In Fig. 1, we show bounds on $1/f_\phi$ from various spectroscopic measurements, particularly the atomic clock comparison tests. All bounds with solid lines are recast either from existing experimental constraints on scalar ultralight dark matter or from the power spectral density of frequency uncertainties. The detailed connection between the constraints on scalar-like dark matter and axion dark matter is discussed in Appendix B. In addition to the clock-comparison tests, we also show the

constraints and projections from the resonant-bar gravitational wave detectors, AURIGA [42], and atom interferometers [41,56,57].

IV. SPECTRUM

The quadratic axion DM signal discussed so far is the harmonic signal, $s(t) \propto \theta^2(t) \propto \cos(2mt)$, at the frequency twice the dark matter mass, $\omega = 2m$. By investigating if the detector output has an oscillating component at $\omega = 2m$ via matched filtering, it is possible to probe or constrain interactions of ULDM with SM particles.

The quadratic operator exhibits not only coherent harmonic oscillations but also distinctive low-frequency stochastic fluctuations at $\omega \lesssim mv^2$, where v denotes the DM velocity. This offers another opportunity to test the QCD axion. Recently, Masia-Roig *et al.* [58] showed that a network of sensors can be used to probe such low-frequency stochastic background in the context of non-gravitational quadratic interactions of ULDM with SM particles. Flambaum and Samsonov [59] argued that, by directly comparing the low-frequency background with experimentally measured uncertainties, it is possible to set limits on the QCD axion parameter space at higher masses.

We provide below the analytic spectrum of the low-frequency fluctuation of the axion dark matter from its quadratic interactions and project the sensitivity of different detector networks.

To see how this low-frequency stochastic noise arises from the quadratic operator, let us assume that the signal is proportional to the quadratic operator as follows,

$$s(t) = K\theta^2(t),$$

with arbitrary constant K. Once we expand the field as[3]

$$\phi(t, x) = \sum_i \frac{1}{\sqrt{2mV}}\left[\alpha_i e^{-ik_i \cdot x} + \alpha_i^* e^{ik_i \cdot x}\right] \quad (10)$$

with complex random numbers (α_i, α_i^*), it is clear that the quadratic operator contains the sum, $\omega_i + \omega_j$, and the difference, $\omega_i - \omega_j$ of two frequencies in the field,

$$\phi^2(t, 0) \supset \alpha_i \alpha_j e^{-i(\omega_i + \omega_j)t} + \alpha_i \alpha_j^* e^{-i(\omega_i - \omega_j)t} + \text{H.c.}$$

In the non-relativistic limit, the first term $\omega_i + \omega_j \simeq 2m$ provides the harmonic signal at $\omega = 2m$. The second term, on the other hand, provides a low-frequency fluctuation at $\omega \lesssim mv^2$.

A more careful investigation is possible via the power spectrum of the quadratic operator. The one-sided power spectral density (PSD) of the signal, $P_s(f)$, is defined as

$$\langle \tilde{s}(f)\tilde{s}^*(f')\rangle = \delta(f - f')\frac{1}{2}P_s(f), \quad (11)$$

where $s(t) = \int df e^{-2\pi ift}\tilde{s}(f)$. Following Ref. [61], for a normal DM velocity distribution $n(\vec{v}) = [(\rho_0/m)/(2\pi\sigma^2)^{3/2}]\exp(-v^2/2\sigma^2)$ with the mean dark matter density ρ_0 and the velocity dispersion σ, one finds the signal PSD as

$$P_s(f) = K^2 \frac{\theta_0^4}{4}\tau_\phi[A(f) + B(f)] \quad (12)$$

where $\tau_\phi = 1/m\sigma^2$ is the coherence time and

$$A(f) = \pi\frac{\bar{v}^4}{\sigma^4}e^{-\bar{v}^2/\sigma^2}\Theta(\bar{v}^2) \quad (13)$$

$$B(f) = 4\bar{\omega}K_1(\bar{\omega}). \quad (14)$$

Here $\bar{v}^2 = 2\pi f/m - 2$, $\bar{\omega} = 2\pi f/m\sigma^2$, $K_n(x)$ is the modified Bessel function of the second kind, and $\Theta(x)$ is the step function. The expression shows two distinctive frequency components: $A(f)$ represents the harmonic signal at $\omega = 2\pi f = 2m$, and $B(f)$ represents the low-frequency stochastic fluctuation. For a detailed derivation, see Appendix C.

The low-frequency stochastic background behaves similarly to white noise and is therefore difficult to distinguish from other random noises in a detector.[4] If it is somehow possible to arrange the output data in a way that it is insensitive to the axion DM signal, then it could be possible to calibrate the noise and therefore detect the axion with only one experiment. Alternatives are the following two approaches: (i) the reported stability of clocks can be used to constrain the parameter space as the low-frequency stochastic DM background would lead to larger fluctuations than the ones observed; (ii) to possibly detect the axion, one may utilize the cross-correlation between multiple experiments for which the individual experiment-intrinsic noise cancels, while the axion signal persists. In the following, we discuss these two possibilities in more detail.

A. Single detector setup

As already demonstrated in Ref. [59], by comparing the low-frequency fluctuations with the measured uncertainty of clocks, one can place lower limits on the decay constant f_ϕ. In a repeated measurement of a given frequency standard, there will be varying fluctuations due to the experiment's intrinsic effects as well as possibly the axion

---

[3]See Appendix C and Refs. [60,61] for more detailed discussions on this statistical description of wave dark matter.

[4]It might be possible to disentangle axion DM-induced fluctuation from Gaussian random noise since axion DM fluctuations from quadratic interaction follows the exponential distribution rather than the normal distribution [59].

signal. Since the low-frequency part of the signal has very similar properties to white noise, we expect the two to be hardly distinguishable. Even if we consider the axion signal as just another component of the noise, we can still constrain the axion by requiring that the noise due to the axion is smaller than the total observed one.

We illustrate this further with the measurement of the frequency ratio of Yb^+ electric-octupole (E3) and electric-quadrupole (E2) clock transitions as an example [36]. As explained above, one way to extract the constraints on $1/f_\phi$ is to directly compare the low-frequency noise $P_s \sim K^2\theta_0^2\tau_\phi$ (12) with the measured clock frequency uncertainties. The fluctuations of the measured frequency ratio in Ref. [36] are consistent with white noise of $P_n(f) = \sigma_n^2 \simeq (10^{-14}/\sqrt{Hz})^2$. A direct comparison leads to the constraint on $1/f_\phi$ as $f_\phi^{-1} = [m^2\sigma_n/(2K\rho_0\sqrt{\tau_\phi})]^{1/2}$ with $K \simeq 10^{-4}$.

The quantity commonly cited to quantify the frequency stability in a clock comparison test is the Allan deviation. [The Allan deviation $\sigma_y(\tau)$ was initially introduced to provide a means to quantify the stability of frequency standards in the presence of noise with a divergent IR behavior. In particular, it describes the stability of frequency between measurements τ-seconds apart.] To find our bounds quantitatively, we compute the Allan deviation caused by the axion DM and require it to be smaller than the experimentally reported value. The Allan deviation is defined in (C20) and the expected value for the axion DM is provided in Appendix C 2. We find

$$\frac{1}{f_\phi} = \left[\frac{m^4\sigma_n^2(\tau)}{8K^2\rho_0^2\mathcal{I}(\tau/2\tau_\phi)}\right]^{1/4} \tag{15}$$

where $\sigma_n(\tau)$ is the reported Allan deviation with an averaging time τ. The detailed derivation and the function $\mathcal{I}(x)$ are given in Appendix C 2. This constraint is shown by the green dashed region in Figs. 1 and 3.

B. Multidetector setup

If two or more detectors are available, it is possible to distinguish the axion DM signal from the detector's noise by cross-correlating multiple detector outputs. Suppose we have two detector outputs $d_{1,2}(t) = s_{1,2}(t) + n_{1,2}(t)$. If we now consider the correlation between the two outputs $\langle d_1 d_2\rangle$, we expect the noises in the two detectors to be uncorrelated among themselves, $\langle n_1 n_2\rangle \sim 0$, while the signal is $\langle s_1 s_2\rangle \neq 0$ as long as the two detectors are placed within one coherence length $L < \lambda \approx 1/(mv)$. In practice, this is done by constructing an observable as $Y = \int dt \int dt' s_1(t)s_2(t')Q(t-t')$ with some real filter function $Q(t-t')$. The signal and noise are computed as $S = \langle Y\rangle$ and $N^2 = [\langle Y^2\rangle - \langle Y\rangle^2]_{s=0}$, respectively. The maximum signal-to-noise ratio is [62]

$$\frac{S}{N} = \left[2T\int_{f_l}^{f_u} df \frac{|P_{cross}|^2}{P_n^2(f)}\right]^{1/2} \tag{16}$$

where $f_{u,l}$ is the highest and lowest frequency where $P_n(f)$ is available, T is the total observation timescale, $P_n(f) = [P_{n_1}(f)P_{n_2}(f)]^{1/2}$ is the noise PSD, and P_{cross} is the cross-correlation defined as

$$\langle \tilde{s}_1(f)\tilde{s}_2^*(f')\rangle = \delta(f-f')\frac{1}{2}P_{cross}(f). \tag{17}$$

For N_{det} detectors, the above expression is modified as $T \to [N_{det}(N_{det}-1)/2]T$ assuming that the noise PSD in all detectors is more or less the same.

The cross-correlation PSD from the axion DM can be computed straightforwardly with the formulation described above. For a normal velocity distribution with zero mean velocity, we find

$$P_{cross}(f,\vec{L}) = K_1 K_2 \frac{\theta_0^4\tau}{4} B_{cross}(f,\vec{L}) \tag{18}$$

where

$$B_{cross}(f,\vec{L}) = 2\int_{-\infty}^{\infty} dx \frac{e^{-i\bar{\omega}x}}{(1+x^2)^{3/2}}\exp\left[-\frac{(m\sigma L)^2}{1+x^2}\right]. \tag{19}$$

Note that $K_{1,2}$ is the sensitivity coefficient defined as $s_i = K_i\theta^2(t)$ and L is the detector separation. The detailed derivation and more general expressions with dark matter mean velocity are given in Appendix C. Note that the above expression coincides with (14) in the $L \to 0$ limit.

In Fig. 3, we choose optical clock systems to investigate to which extent they can probe the QCD axion parameter space at a higher mass range. Assuming only white noise and $m\sigma L \ll 1$ such that $B_{cross} \approx B$, one finds the projected sensitivity on $1/f_\phi$ as
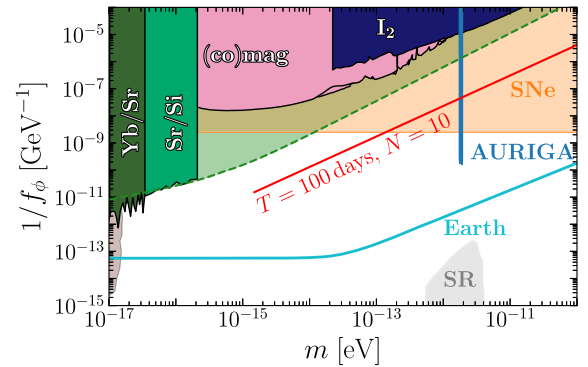
FIG. 3. A projection for cross-correlation with optical clock systems (red line). We choose $T = 100$ days, $N_{det} = 10$ detectors, and $S/N = 3$.

$$\frac{1}{f_\phi} \approx \left[\frac{P_n}{4K_1K_2}\frac{S}{N}\frac{m^4}{\rho_0^2}\right]^{\frac{1}{4}}\left[\frac{\pi}{T\tau_\phi \min(1, 2\pi f_u \tau_\phi)}\right]^{\frac{1}{8}} \quad (20)$$

We choose $K_{1,2} = 10^{-4}$, measurement frequency $f_u = 1$ Hz, and $P_n^{1/2}(f) = 10^{-16}/\sqrt{\text{Hz}}$. Unlike the single detector setup in the previous section, the signal-to-noise ratio and the projection on $1/f_\phi$ show a mild improvement as a function of observation time and the number of detectors. This can be seen by comparing the projection of a network with $T = 100$ days and $N_{\text{det}} = 10$ detectors shown in Fig. 3 as a red line, with the green dashed region showing the Yb^+ (E3)/(E2) constraint from the previous section in a single detector setup. Crucially the multidetector setup allows for the detection of the axion since the nonvanishing cross-correlation can distinguish the signal from detector noise.

[Before we conclude, we remark on the parameter space shown in the figures. We consider an axion that couples to the gluon field (1), while we have treated the mass m and the decay constant f_ϕ as if they are independent. These two parameters are not independent in minimal QCD axion models, as QCD provides an inevitable mass contribution to the axion; the axion mass is given as $m^2 \sim \Lambda_{\text{QCD}}^4/f_\phi^2$. As a result, the parameter space above the olive line in Fig. 1 cannot be achieved by minimal QCD axion scenarios. However, it was recently shown that this parameter space with small mass can be achieved in a technically natural way by introducing a discrete symmetry [63] and can also be dark matter in the present universe [64].]

V. CONCLUSION

In this work, we have considered the quadratic interactions of the QCD axion with the electromagnetic field and the electron mass. These quadratic interactions naturally arise as long as the axion couples to the gluon field of the standard model. Similar to the quadratic interaction with pions and nucleons, such interactions lead to oscillating atomic energy levels. Contrary to the hadronic coupling, the electromagnetic interaction directly affects the electronic energy levels, making systems that depend on these energy levels sensitive to axion DM. As examples of such systems, we studied optical clocks, resonant-bar gravitational wave detectors, and atom interferometers.

We have summarized existing constraints and projected sensitivities of future nuclear clocks in Fig. 1. While they are still far from the minimal QCD axion parameter space, they provide alternative ways to search the QCD axion. Moreover, the quadratic nature inevitably introduces a low-frequency stochastic background. We have derived an analytic expression for the low-frequency spectrum of the ultralight DM-induced signal. By directly comparing the axion DM-induced low-frequency fluctuations with measured clock uncertainties, we show that the Yb^+ (E3) and (E2) comparison can also probe heavier axions than those considered in previous work [36]. In addition, with several assumptions, we have also projected the sensitivity of a network of detectors, which could probe this higher mass range further.

Note added. While this work was being finalized, a related work [65] appeared on the arXiv, which shares some of the points discussed above.

APPENDIX A: CLOCK COMPARISON TEST

We list the sensitivity coefficient for the QCD axion for different atomic species. Let us consider the frequency standards based on hyperfine and electronic transitions. The transition frequency is parametrized as

$$f_{\text{hfs}} = g\frac{m_e^2}{m_p}\alpha^4 F_{\text{hfs}}(\alpha), \quad (A1)$$

$$f_{\text{elec}} = m_e\alpha^2 F_{\text{elec}}(\alpha), \quad (A2)$$

where g is the nuclear g-factor, and $F(\alpha)$ is the relativistic correction.

There are total 4 parameters, $\{g, m_e, m_p, \alpha\}$. Each of them varies in time. The transition frequency can be conveniently written as $f_A = g_A^{K_g}m_e^{K_{m_e}}m_p^{K_{m_p}}\alpha^{K_\alpha}$. Since the effect of the QCD axion always arises through the variation of pion mass, the fractional frequency change can be written as

$$\frac{\delta f_A}{f_A} = \sum_i K_i \frac{\partial \ln A_i}{\partial \ln m_\pi^2}\frac{\delta m_\pi^2}{m_\pi^2} \quad (A3)$$

where the index runs over all four parameters. $K_g = 1, 0$, $K_{m_e} = 2, 1$, and $K_{m_p} = -1, 0$ for hyperfine and electronic transition, respectively. The values for K_α can be found in Refs. [66,67]. The dependence of each parameter on the pion mass is

$$\frac{\partial \ln m_p}{\partial \ln m_\pi^2} = \frac{\sigma_{\pi N}}{m_N} \simeq 0.06 \quad (A4)$$

TABLE I. Table for the sensitivity coefficient K_A for the QCD axion. The electromagnetic quadratic interactions provide the dominant effect for the optical clock transitions, while the hadronic couplings provide the dominant effects for hyperfine and nuclear clock transitions.

System	Transition	K_A
H	Ground state hyperfine	$+1.2 \times 10^{-2}$
Cs	Ground state hyperfine	$+2.6 \times 10^{-3}$
Rb	Ground state hyperfine	$+4.5 \times 10^{-3}$
Si	Cavity	-1.5×10^{-5}
Sr	$^1S_0 \to {}^3P_0$	-3.2×10^{-5}
Al$^+$	$^1S_0 \to {}^3P_0$	-3.1×10^{-5}
Hg$^+$	$^2S_{1/2} \to {}^2D_{5/2}$	$+1.4 \times 10^{-5}$
Yb	$^1S_0 \to {}^3P_0$	-3.5×10^{-5}
Yb$^+$ (E2)	$^2S_{1/2} \to {}^2D_{3/2}$	-4.6×10^{-5}
Yb$^+$ (E3)	$^2S_{1/2} \to {}^2F_{7/2}$	$+6.0 \times 10^{-5}$
Th	Nuclear	-2.2×10^4

$$\frac{\partial \ln \alpha}{\partial \ln m_\pi^2} = \frac{\alpha}{12\pi}\left(1 + \frac{8\sigma_{\pi N}}{m_N}\right) \simeq 3 \times 10^{-4} \qquad \text{(A5)}$$

$$\frac{\partial \ln m_e}{\partial \ln m_\pi^2} = \frac{3\alpha^2}{48\pi^2}\left(1 + \frac{8\sigma_{\pi N}}{m_N}\right)\ln\frac{m_\pi^2}{m_e^2} \simeq 6 \times 10^{-6}. \qquad \text{(A6)}$$

where $\sigma_{\pi N} = \partial m_N/\partial \ln m_\pi^2$. For the g-factor, one finds $\partial \ln g_p / \partial \ln m_\pi^2 = -(g_A^2/g_p)[m_N m_\pi/(8\pi f_\pi^2)] \simeq -0.17$ for the hydrogen atom, $\partial \ln g_{\rm Rb}/\partial \ln m_\pi^2 = -0.024$ for ^{87}Rb, and $\partial \ln g_{\rm Cs}/\partial \ln m_\pi^2 = 0.011$ for ^{133}Cs [31]. For the nuclear clock transition in ^{229}Th, the hadronic quadratic coupling is dominant, $\delta f_A/f_A \simeq (2 \times 10^5) \times \delta m_\pi^2/m_\pi^2$ [31].

The above expression can be written in a more compact form:

$$\frac{\delta f_A}{f_A} = K_A \theta^2. \qquad \text{(A7)}$$

The sensitivity coefficient K_A for each system is listed in Table I. The sensitivity coefficient of the frequency ratio of any pair of atomic transitions is simply the difference of the two respective sensitivity coefficients.

APPENDIX B: RECASTING LIMITS

For the deterministic signal search at $\omega = 2m$, the previous results on dilaton dark matter can be straightforwardly converted into the constraints on axion dark matter. We illustrate this with the electromagnetic couplings of dilaton dark matter, parametrized as

$$\mathcal{L} = \frac{\phi}{\sqrt{2}M_p}\frac{d_e}{4}F_{\mu\nu}F^{\mu\nu}, \qquad \text{(B1)}$$

where M_p is the reduced Planck mass. This leads to a fluctuation in the fine structure constant as

$$\frac{\delta\alpha}{\alpha} = \frac{d_e\phi_0}{\sqrt{2}M_p}\cos(mt) \qquad \text{(B2)}$$

where $\phi \approx \phi_0 \cos(mt)$ with $\phi_0 = \sqrt{2\rho}/m$.

Consider now two frequency standards A and B. Suppose that they are proportional to the fine structure constant as $f_{A,B} \propto \alpha^{\xi_A, \xi_B}$. The fractional frequency uncertainty due to the dilaton dark matter is then given by

$$s(t) \equiv \frac{\delta(f_A/f_B)}{f_A/f_B} = (\xi_A - \xi_B)\frac{\delta\alpha}{\alpha}$$
$$= (\xi_A - \xi_B)\frac{d_e\sqrt{\rho}}{mM_p}\cos(mt). \qquad \text{(B3)}$$

The dilaton-induced signal appears at $\omega = m$. On the other hand, the fractional uncertainty due to the axion dark matter is

$$s(t) \equiv \frac{\delta(f_A/f_B)}{f_A/f_B} = (K_A - K_B)\theta^2$$
$$\approx (K_A - K_B)\frac{\rho}{m^2 f_\phi^2}\cos(2mt) \qquad \text{(B4)}$$

where we have dropped the constant term. The axion-induced signal appears at $\omega = 2m$.

Carefully considering the difference in the frequency of time-oscillating signal, the constraints on dilaton couplings $d_e(2m)$ at the dilaton mass $2m$ can be translated into the constraints on $1/f_\phi(m)$ at the axion mass m:

$$\frac{1}{f_\phi(m)} = \left[\frac{\xi_A - \xi_B}{K_A - K_B}\frac{m}{2M_p}\frac{d_e(2m)}{\sqrt{\rho}}\right]^{1/2}. \qquad \text{(B5)}$$

We emphasize that $f_\phi(m)$ is the resulting constraint on the decay constant at the axion mass m, while $d_e(2m)$ is the constraint on the linear dilaton-photon coupling at the dilaton mass $2m$. Using this relation, previous constraints on d_e of the dilaton dark matter can easily be translated into the constraints on axion parameter space. While we demonstrate this connection with d_e, the discussion equally applies to other linear couplings of dilaton dark matter.

APPENDIX C: QUADRATIC SPECTRUM

Here we provide a detailed computation of the low-frequency power spectrum, following Ref. [61].

We expand the field as

$$\phi(t,x) = \sum_i \frac{1}{\sqrt{2mV}}\left[\alpha_i e^{-ik_i \cdot x} + \alpha_i^* e^{ik_i \cdot x}\right]. \qquad \text{(C1)}$$

Here (α_i, α_i^*) are complex random numbers. The underlying probability distribution of this complex random number is given by [60,68–70]

$$p(\alpha_i) = \frac{1}{\pi n_i} e^{-|\alpha_i|^2/n_i}, \tag{C2}$$

where n_i is the mean occupation number of the mode i. The probability of finding α_i in $[\alpha_i, \alpha_i + d\alpha_i]$ is

$$dP = p(\alpha_i)d^2\alpha_i = [p(r_i)dr_i][p(\phi_i)d\phi_i] \tag{C3}$$

where $\alpha_i = r_i e^{i\phi_i}$, $d^2\alpha_i = r_i dr_i d\phi_i$, and

$$p(r_i) = \frac{2r_i}{n_i} e^{-r_i^2/n_i}, \tag{C4}$$

$$p(\phi_i) = \frac{1}{2\pi}. \tag{C5}$$

The amplitude $r_i = |\alpha_i|$ follows the Rayleigh distribution, while the phase ϕ_i is uniformly distributed. In this description, the field ϕ is a Gaussian random field.

The mean occupation number n_i is given by the dark matter velocity distribution. For simplicity, we assume a normal distribution

$$n(\vec{v}) = \frac{\rho_0/m}{(2\pi\sigma^2)^{3/2}} \exp\left[-\frac{(\vec{v} - \vec{v}_0)^2}{2\sigma^2}\right] \tag{C6}$$

where ρ_0 is the mean dark matter density, $\vec{v}_0$ is the velocity of the dark matter wind relative to the experiment, and σ is the velocity dispersion.

We focus on the case where the signal in the detector is of the following form:

$$s(t) = K\theta^2(t), \tag{C7}$$

where K is a sensitivity coefficient and $\theta = \phi/f_\phi$. The power spectral density $P_s(f)$ is defined as

$$\langle \tilde{s}(f)\tilde{s}^*(f')\rangle = \delta(f - f')\frac{1}{2}P_s(f). \tag{C8}$$

We choose the following convention for the Fourier transformation, $s(t) = \int df e^{-2\pi i f t}\tilde{s}(f)$.

The signal power spectral density is related to the PSD of the axion field as

$$P_s(f) = K^2 P_{\delta\theta^2}(f) \tag{C9}$$

where

$$\langle \widetilde{\delta\theta^2}(f)\widetilde{\delta\theta^2}^*(f')\rangle = \delta(f - f')\frac{1}{2}P_{\delta\theta^2}(f). \tag{C10}$$

We have introduced $\delta\theta^2 = \theta^2 - \langle\theta^2\rangle$. This subtracts an unobservable constant shift in θ^2. Note that the above power spectrum is one-sided; we only consider $f \geq 0$.

1. Power spectral density

The Fourier component of the quadratic operator is

$$\widetilde{\theta^2}(\omega) = \frac{1}{f_\phi^2}\frac{1}{2mV}\sum_{i,j}\Big[\alpha_i\alpha_j e^{i(\vec{k}_i+\vec{k}_j)\cdot\vec{x}}(2\pi)\delta(\omega - \omega_i - \omega_j)$$
$$+ \alpha_i\alpha_j^* e^{i(\vec{k}_i-\vec{k}_j)\cdot\vec{x}}(2\pi)\delta(\omega - \omega_i + \omega_j)$$
$$+ \alpha_i^*\alpha_j e^{-i(\vec{k}_i-\vec{k}_j)\cdot\vec{x}}(2\pi)\delta(\omega + \omega_i - \omega_j)$$
$$+ \alpha_i^*\alpha_j^* e^{-i(\vec{k}_i+\vec{k}_j)\cdot\vec{x}}(2\pi)\delta(\omega + \omega_i + \omega_j)\Big] \tag{C11}$$

To compute $\langle\widetilde{\delta\theta^2}(\omega)\widetilde{\delta\theta^2}^*(\omega')\rangle$, the following expression is useful

$$\langle\alpha_i\alpha_j\alpha_k^*\alpha_l^*\rangle = n_i n_j(\delta_{ik}\delta_{jl} + \delta_{il}\delta_{jk}). \tag{C12}$$

The angle bracket denotes an ensemble average, defined as

$$\langle\mathcal{O}\rangle = \int\left[\prod_i d^2\alpha_i p(\alpha_i)\right]\mathcal{O}. \tag{C13}$$

After a straightforward computation, we find

$$P_{\delta\theta^2}(\omega) = \frac{1}{m^2 f_\phi^4}\int d^3v_1 d^3v_2 n(\vec{v}_1)n(\vec{v}_2)$$
$$\times\big[(2\pi)\delta(\omega - \omega_1 - \omega_2) + (2\pi)\delta(\omega + \omega_1 + \omega_2)$$
$$+ (2\pi)\delta(\omega - \omega_1 + \omega_2) + (2\pi)\delta(\omega + \omega_1 - \omega_2)\big], \tag{C14}$$

where we took the continuum limit in the velocities. This is a general expression, which holds for an arbitrary velocity distribution as long as the probability distribution for α_i is given as (C2).

Given a normal velocity distribution (C6), we find that the power spectrum of the scalar quadratic operator is

$$P_{\delta\theta^2}(f) = \frac{1}{4}\theta_0^4\tau_\phi[A(f) + B(f)], \tag{C15}$$

where $\theta_0 = \sqrt{2\rho_0}/mf_\phi$, $\tau_\phi = 1/m\sigma^2$ is the coherence time, and

$$A(f) = \frac{2\pi\bar{v}^2}{v_0^2}\exp\left[-\frac{\bar{v}^2 + v_0^2}{\sigma^2}\right]I_2\left(\frac{2v_0\bar{v}}{\sigma^2}\right)\Theta(\bar{v}^2), \tag{C16}$$

$$B(f) = \frac{2\sigma}{v_0}\int_0^\infty dv_c e^{-\frac{\bar{\omega}^2}{4v_c^2}}\left[e^{-(v_c - \frac{v_0}{\sigma})^2} - e^{-(v_c + \frac{v_0}{\sigma})^2}\right]. \tag{C17}$$

Here $I_n(x)$ is the modified Bessel function of the first kind and $\Theta(x)$ is the unit step function. For notational simplicity, we have introduced
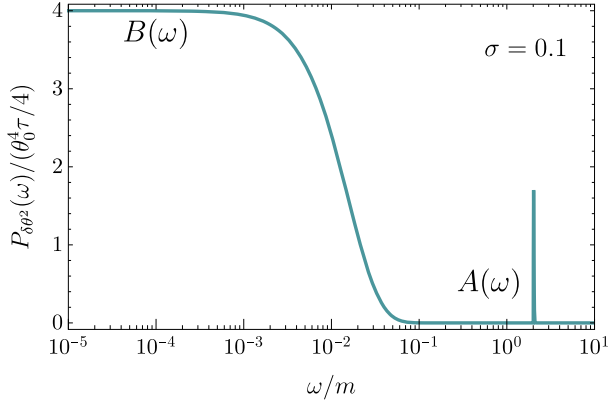
FIG. 4. The spectrum of the quadratic operator $\delta\theta^2$ in the isotropic limit. We choose $\sigma = 0.1$ for demonstration. The narrow peak at $\omega = 2m$ represents the harmonic oscillations, while the plateau at $\omega < m\sigma^2$ gives the low-frequency stochastic background.

$$\bar{v}^2 = \frac{2\pi f}{m} - 2, \quad \text{and} \quad \bar{\omega} = \frac{2\pi f}{m\sigma^2}.$$

The spectral function $A(f)$ represents the coherent harmonic oscillation at $\omega = 2m$. The spectral function $B(f)$ represents the low-frequency background at $\omega < m\sigma^2$. Note that the above PSD is valid for $f > 0$. The low-frequency spectrum $B(f)$ is still valid for $f < 0$, but $A(f)$ changes to $A(-f)$.

These expressions are further simplified in the isotropic limit $v_0 \to 0$. In this case, we find

$$A(f) = \pi \frac{\bar{v}^4}{\sigma^4} e^{-\bar{v}^2/\sigma^2} \Theta(\bar{v}^2), \tag{C18}$$

$$B(f) = 4\bar{\omega}K_1(\bar{\omega}), \tag{C19}$$

where $K_n(x)$ is the modified Bessel function of the second kind and $\Theta(x)$ is the step function. Note that both functions, A and B, are normalized such that $\tau_\phi \int_0^\infty df A(f) = \tau_\phi \int_0^\infty df B(f) = 1$. The spectrum in this case is shown in Fig. 4.

2. Allan deviation

Let us consider a single clock comparison test in which the axion causes a signal $s(t) = K\delta\theta^2(t)$. If this signal cannot be distinguished from the noise, it still contributes to the total observed variation of the frequencies commonly characterized by the Allan deviation. In terms of the fractional frequency shift, the Allan variance over a period $\tau = n \cdot \Delta t$, where Δt is the time between measurements, is defined as [71]

$$\sigma_s^2(\tau) = \frac{1}{2(M-1)} \sum_{i=1}^{M-1} |\langle s(\tau)\rangle_{i+1} - \langle s(\tau)\rangle_i|^2, \tag{C20}$$

where $\langle s(\tau)\rangle_i$ denotes the i-th measurement of $s(t)$ over the period τ,

$$\langle s(\tau)\rangle_i = \frac{1}{\bar{t}} \int_{t_i}^{t_i+\tau} dt s(t) = K\overline{\delta\theta^2}(t_i). \tag{C21}$$

In the second step, we defined $\overline{\delta\theta^2}(t_i)$ as the average value of $\delta\theta^2$ over this period. The ensemble average of the Allan variance then becomes

$$\langle \sigma_s^2(\tau)\rangle = \frac{K^2}{2(M-1)}$$

$$\times \sum_{i=1}^{M-1} \left\langle \left| \int df(e^{-2\pi i f(t_i+\tau)} - e^{-2\pi i f t_i})\widetilde{\overline{\delta\theta^2}}(f) \right|^2 \right\rangle$$

$$= 2K^2 \int_0^\infty df \sin^2(\pi f\tau) P_{\overline{\delta\theta^2}}(f). \tag{C22}$$

Here the angle bracket denotes an ensemble average. The Fourier transformation and power spectrum of $\overline{\delta\theta^2}$ are defined analogously to the ones of $\delta\theta^2$. To find the relation between these quantities let us consider the Fourier transformation

$$\widetilde{\overline{\delta\theta^2}}(f) = \int dt e^{2\pi i t f}\left[\frac{1}{\tau}\int_t^{t+\tau} dt' \delta\theta^2(t')\right] \tag{C23}$$

$$= e^{-\pi i f t}\text{sinc}(\pi f\tau)\widetilde{\delta\theta^2}(f), \tag{C24}$$

where $\text{sinc}(x) = \sin(x)/x$. The two power spectra are therefore simply related by a factor $\text{sinc}^2(\pi f\tau)$, i.e. $P_{\overline{\delta\theta^2}}(f) = \text{sinc}^2(\pi f\tau)P_{\delta\theta^2}(f)$. Using this, we find

$$\langle \sigma_s^2(\tau)\rangle = 2K^2 \int_0^\infty df P_{\delta\theta^2}(f)\frac{\sin^4(\pi f\tau)}{(\pi f\tau)^2}. \tag{C25}$$

From this expression, the Allan deviation caused by the quadratic coupling can be computed using the coupling coefficients that can be found in Table I and the power spectral density from the last section. In particular, in the isotropic limit, we find

$$\langle \sigma_s^2(\tau)\rangle = 2K^2\theta_0^4 \mathcal{I}(\tau/2\tau_\phi) \tag{C26}$$

with the integral $\mathcal{I}(x)$ defined as

$$\mathcal{I}(x) = \int_0^\infty \frac{d\bar{\omega}}{2\pi}\bar{\omega}K_1(\bar{\omega})\frac{\sin^4(\bar{\omega}x)}{(\bar{\omega}x)^2}. \tag{C27}$$

The constraint on $1/f_\phi$ is therefore obtained as

$$\frac{1}{f_\phi} = \left[\frac{m^4\sigma_{s,\text{obs}}^2(\tau)}{8K^2\rho_0^2\mathcal{I}(\tau/2\tau_\phi)}\right]^{1/4} \tag{C28}$$

where $\sigma_{s,\text{obs}}(\tau)$ is the experimentally measured Allan deviation with an averaging time τ.

We obtain the bound shown in Figs. 1 and 3 as a green dashed region, by requiring that the noise caused by the coupling of the axion is below the 1σ upper bound on the Allan deviation shown in Fig. 1 of [36] for all given values of τ.

3. Cross-correlation

Above we computed the correlation between $\delta\theta^2(\omega)$ evaluated at the same spatial position. For the cross-correlation of displaced detectors, we must evaluate $\delta\theta^2(\omega)$ at different spatial positions. In particular, we are interested in

$$\langle \widetilde{\delta\theta^2}_a(\omega)\widetilde{\delta\theta^2}^*_b(\omega') \rangle = (2\pi)\delta(\omega-\omega')\frac{1}{2}P^{\text{cross}}_{\delta\theta^2}(\omega,\vec{L}). \quad \text{(C29)}$$

where $\widetilde{\delta\theta^2}_a(\omega) = \widetilde{\delta\theta^2}(\omega,\vec{x}_a)$ and $\vec{L} = \vec{x}_a - \vec{x}_b$ is the distance between two detectors. Following the same line of computation, we find

$$P^{\text{cross}}_{\delta\theta^2}(\omega,\vec{L}) = \frac{1}{m^2 f_\phi^4}\int d^3v_1 d^3v_2 n(\vec{v}_1)n(\vec{v}_2)$$

$$\times \Big[(2\pi)\delta(\omega-\omega_1-\omega_2)e^{+i(\vec{k}_1+\vec{k}_2)\cdot\vec{L}}$$

$$+ (2\pi)\delta(\omega+\omega_1+\omega_2)e^{-i(\vec{k}_1+\vec{k}_2)\cdot\vec{L}}$$

$$+ (2\pi)\delta(\omega-\omega_1+\omega_2)e^{+i(\vec{k}_1-\vec{k}_2)\cdot\vec{L}}$$

$$+ (2\pi)\delta(\omega+\omega_1-\omega_2)e^{-i(\vec{k}_1-\vec{k}_2)\cdot\vec{L}} \Big] \quad \text{(C30)}$$

Assuming the normal velocity distribution (C6), we find

$$P^{\text{cross}}_{\delta\theta^2}(f,\vec{L}) = \frac{1}{4}\theta_0^2\tau\big[A_{\text{cross}}(f,\vec{L}) + B_{\text{cross}}(f,\vec{L})\big] \quad \text{(C31)}$$

where the two spectral functions are given by

$$A_{\text{cross}}(f) = \frac{2\pi(\bar{v}/\sigma)^2}{X^2}\exp\left[-\frac{\bar{v}^2+v_0^2}{\sigma^2}\right]I_2\left(2X\frac{\bar{v}}{\sigma}\right)\theta(\bar{v}^2) \quad \text{(C32)}$$

$$B_{\text{cross}}(f) = 2\int_{-\infty}^{\infty}ds\,\frac{e^{-i\bar{\omega}s}}{(1+s^2)^{3/2}}\exp\left[-\frac{(\vec{L}_\lambda + s\frac{\vec{v}_0}{\sigma})^2}{1+s^2}\right] \quad \text{(C33)}$$

Here $\vec{X} = \vec{v}_0/\sigma + i\vec{L}_\lambda$ with $\vec{L}_\lambda = m\sigma\vec{L}$ is introduced. These expressions reduce to (C18)–(C19) in the isotropic $v_0 \to$ and small distance $L \to 0$ limit. This expression is valid again for $f > 0$. The low-frequency spectrum $B_{\text{cross}}(f,\vec{L})$ is valid also for $f < 0$, but the other component $A_{\text{cross}}(f,\vec{L})$ changes for $f < 0$ to $A_{\text{cross}}(f,\vec{L}) \to A_{\text{cross}}(-f,-\vec{L})$.

[1] R. D. Peccei and H. R. Quinn, Phys. Rev. Lett. **38**, 1440 (1977).

[2] R. D. Peccei and H. R. Quinn, Phys. Rev. D **16**, 1791 (1977).

[3] S. Weinberg, Phys. Rev. Lett. **40**, 223 (1978).

[4] F. Wilczek, Phys. Rev. Lett. **40**, 279 (1978).

[5] J. E. Kim, Phys. Rev. Lett. **43**, 103 (1979).

[6] M. A. Shifman, A. I. Vainshtein, and V. I. Zakharov, Nucl. Phys. **B166**, 493 (1980).

[7] A. R. Zhitnitsky, Sov. J. Nucl. Phys. **31**, 260 (1980).

[8] M. Dine, W. Fischler, and M. Srednicki, Phys. Lett. **104B**, 199 (1981).

[9] C. D. Froggatt and H. B. Nielsen, Nucl. Phys. **B147**, 277 (1979).

[10] F. Piazza and M. Pospelov, Phys. Rev. D **82**, 043533 (2010).

[11] P. W. Graham, D. E. Kaplan, and S. Rajendran, Phys. Rev. Lett. **115**, 221801 (2015).

[12] A. Arvanitaki, S. Dimopoulos, V. Gorbenko, J. Huang, and K. Van Tilburg, J. High Energy Phys. 05 (2017) 071.

[13] A. Banerjee, H. Kim, and G. Perez, Phys. Rev. D **100**, 115026 (2019).

[14] A. Banerjee, H. Kim, O. Matsedonskyi, G. Perez, and M. S. Safronova, J. High Energy Phys. 07 (2020) 153.

[15] N. Arkani-Hamed, R. T. D'Agnolo, and H. D. Kim, Phys. Rev. D **104**, 095014 (2021).

[16] R. Tito D'Agnolo and D. Teresi, Phys. Rev. Lett. **128**, 021803 (2022).

[17] R. Tito D'Agnolo and D. Teresi, J. High Energy Phys. 02 (2022) 023.

[18] A. Chatrchyan and G. Servant, J. Cosmol. Astropart. Phys. 06 (2023) 036.

[19] E. G. Adelberger, B. R. Heckel, and A. E. Nelson, Annu. Rev. Nucl. Part. Sci. **53**, 77 (2003).

[20] J. Bergé, P. Brax, G. Métris, M. Pernot-Borràs, P. Touboul, and J.-P. Uzan, Phys. Rev. Lett. **120**, 141101 (2018).

[21] J. Preskill, M. B. Wise, and F. Wilczek, Phys. Lett. **120B**, 127 (1983).

[22] L. F. Abbott and P. Sikivie, Phys. Lett. **120B**, 133 (1983).

[23] M. Dine and W. Fischler, Phys. Lett. **120B,** 137 (1983).
[24] W. Hu, R. Barkana, and A. Gruzinov, Phys. Rev. Lett. **85,** 1158 (2000).
[25] L. Hui, Annu. Rev. Astron. Astrophys. **59,** 247 (2021).
[26] A. Banerjee, G. Perez, M. Safronova, I. Savoray, and A. Shalit, J. High Energy Phys. 10 (2023) 042.
[27] A. Hook and J. Huang, J. High Energy Phys. 06 (2018) 036.
[28] R. Balkin, J. Serra, K. Springmann, and A. Weiler, J. High Energy Phys. 07 (2020) 221.
[29] J. Zhang, Z. Lyu, J. Huang, M. C. Johnson, L. Sagunski, M. Sakellariadou, and H. Yang, Phys. Rev. Lett. **127,** 161101 (2021).
[30] R. Balkin, J. Serra, K. Springmann, S. Stelzl, and A. Weiler, arXiv:2211.02661.
[31] H. Kim and G. Perez, Phys. Rev. D **109,** 015005 (2024).
[32] A. Hees, J. Guéna, M. Abgrall, S. Bize, and P. Wolf, Phys. Rev. Lett. **117,** 061301 (2016).
[33] C. J. Kennedy, E. Oelker, J. M. Robinson, T. Bothwell, D. Kedar, W. R. Milner, G. E. Marti, A. Derevianko, and J. Ye, Phys. Rev. Lett. **125,** 201302 (2020).
[34] N. Sherrill *et al.*, New J. Phys. **25,** 093012 (2023).
[35] K. Beloy *et al.* (Boulder Atomic Clock Optical Network Bacon Collaboration), Nature (London) **591,** 564 (2021).
[36] M. Filzinger, S. Dörscher, R. Lange, J. Klose, M. Steinel, E. Benkler, E. Peik, C. Lisdat, and N. Huntemann, Phys. Rev. Lett. **130,** 253001 (2023).
[37] I. M. Bloch, Y. Hochberg, E. Kuflik, and T. Volansky, J. High Energy Phys. 01 (2020) 167.
[38] I. M. Bloch, G. Ronen, R. Shaham, O. Katz, T. Volansky, and O. Katz (NASDUCK Collaboration), Sci. Adv. **8,** abl8919 (2022).
[39] J. Lee, M. Lisanti, W. A. Terrano, and M. Romalis, Phys. Rev. X **13,** 011050 (2023).
[40] K. Wei *et al.*, arXiv:2306.08039.
[41] D. Aybas *et al.*, Phys. Rev. Lett. **126,** 141802 (2021).
[42] A. Branca, M. Bonaldi, M. Cerdonio, L. Conti, P. Falferi, F. Marin, R. Mezzena, A. Ortolan, G. A. Prodi, L. Taffarello, G. Vedovato, A. Vinante, S. Vitale, and J.-P. Zendri, Phys. Rev. Lett. **118,** 021302 (2017).
[43] C. Abel *et al.*, Phys. Rev. X **7,** 041034 (2017).
[44] G. G. Raffelt, Lect. Notes Phys. **741,** 51 (2008).
[45] A. Arvanitaki, M. Baryakhtar, and X. Huang, Phys. Rev. D **91,** 084011 (2015).
[46] A. Arvanitaki, J. Huang, and K. Van Tilburg, Phys. Rev. D **91,** 015015 (2015).

[47] I. Kozyryev, Z. Lasner, and J. M. Doyle, Phys. Rev. A **103,** 043313 (2021).
[48] D. Budker, J. Eby, M. Gorghetto, M. Jiang, and G. Perez, J. Cosmol. Astropart. Phys. 12 (2023) 021.
[49] G. Grilli di Cortona, E. Hardy, J. Pardo Vega, and G. Villadoro, J. High Energy Phys. 01 (2016) 034.
[50] P. Di Vecchia and G. Veneziano, Nucl. Phys. **B171,** 253 (1980).
[51] L. Ubaldi, Phys. Rev. D **81,** 025011 (2010).
[52] M. Hoferichter, J. Ruiz de Elvira, B. Kubis, and U.-G. Meißner, Phys. Rev. Lett. **115,** 192301 (2015).
[53] Y. V. Stadnik and V. V. Flambaum, Phys. Rev. Lett. **115,** 201301 (2015).
[54] Y. V. Stadnik and V. V. Flambaum, Phys. Rev. A **94,** 022111 (2016).
[55] A. Banerjee, D. Budker, M. Filzinger, N. Huntemann, G. Paz, G. Perez, S. Porsev, and M. Safronova, arXiv:2301.10784.
[56] P. W. Graham, D. E. Kaplan, J. Mardon, S. Rajendran, and W. A. Terrano, Phys. Rev. D **93,** 075029 (2016).
[57] A. Arvanitaki, P. W. Graham, J. M. Hogan, S. Rajendran, and K. Van Tilburg, Phys. Rev. D **97,** 075020 (2018).
[58] H. Masia-Roig *et al.*, Phys. Rev. D **108,** 015003 (2023).
[59] V. V. Flambaum and I. B. Samsonov, Phys. Rev. D **108,** 075022 (2023).
[60] H. Kim and A. Lenoci, Phys. Rev. D **105,** 063032 (2022).
[61] H. Kim, J. Cosmol. Astropart. Phys. 12 (2023) 018.
[62] M. Maggiore, *Gravitational Waves. Vol. 1: Theory and Experiments* (Oxford University Press, New York, 2007).
[63] A. Hook, Phys. Rev. Lett. **120,** 261802 (2018).
[64] L. Di Luzio, B. Gavela, P. Quilez, and A. Ringwald, J. Cosmol. Astropart. Phys. 10 (2021) 001.
[65] C. Beadle, S. A. R. Ellis, J. Quevillon, and P. N. H. Vuong, arXiv:2307.10362.
[66] V. V. Flambaum and A. F. Tedesco, Phys. Rev. C **73,** 055501 (2006).
[67] M. S. Safronova, D. Budker, D. DeMille, D. F. J. Kimball, A. Derevianko, and C. W. Clark, Rev. Mod. Phys. **90,** 025008 (2018).
[68] A. Derevianko, Phys. Rev. A **97,** 042506 (2018).
[69] J. W. Foster, N. L. Rodd, and B. R. Safdi, Phys. Rev. D **97,** 123006 (2018).
[70] G. P. Centers *et al.*, Nat. Commun. **12,** 7321 (2021).
[71] A. D. Ludlow, M. M. Boyd, J. Ye, E. Peik, and P. O. Schmidt, Rev. Mod. Phys. **87,** 637 (2015).